Surface & Coatings Technology 452 (2023) 129130

Contents lists available at ScienceDirect

Surface & Coatings Technology

journal homepage: www.elsevier.com/locate/surfcoat

Improving the surface properties of additive-manufactured Inconel 625 by plasma nitriding

Danijela A. Skobir Balantič, Črtomir Donik, Bojan Podgornik, Aleksandra Kocijan, Matjaž Godec *

Institute of Metals and Technology, Lepi pot 11, 1000 Ljubljana, Slovenia

A R T I C L E I N F O

Keywords:
Additive manufacturing
Powder-bed fusion
Plasma nitriding
Expanded austenite
Wear and corrosion resistance
Ni-based alloy

A B S T R A C T

As a surface-hardening technique, plasma nitriding is a common procedure for improving the properties of conventional Ni-based alloys. The diffusion of nitrogen hardens a layer on the surface of the alloy, leading to better wear resistance and a higher coefficient of friction, as well as a higher surface hardness. This study reports the effect of plasma nitriding on additive-manufactured (AM) Inconel 625 (IN625) compared to its conventional manufactured and nitrided counterparts. The samples produced with the laser powder-bed fusion (LPBF) process were subsequently plasma nitrided in the as-built condition, stress-relief annealed at 870 °C and solution treated at 1050 °C. The plasma nitridings were carried out at 430 °C and 500 °C for 15 h. The growth kinetics of the nitride layer of the AM samples depends on the prior heat treatments and is faster in the as-built state due to the specific cellular structure. The lower nitriding temperature leads to the formation of expanded austenite in the nitride layer, while at the higher nitriding temperature, the expanded austenite decomposes and CrN precipitation occurs. The XRD and SEM analyses confirmed the presence of two layers: the surface layer and the diffusion layer beneath. The lower nitriding temperature caused the formation of expanded austenite or a combination of expanded austenite and CrN. The higher nitriding temperature led to the decomposition of the expanded austenite and to the formation/precipitation of CrN. The higher nitriding temperature also decreased the corrosion resistance slightly due to the increased number of precipitated Cr-nitrides. On the other hand, the wear resistance was significantly improved after plasma nitriding and was much less influenced by the nitriding temperature.

1. Introduction

Inconel 625 (IN625) belongs to the group of nickel-based superalloys containing a large amount of chromium. It possesses superior mechanical properties, such as high-temperature strength and high creep resistance, obtained by solid solution strengthening, involving the alloying elements Mo and Nb in the Ni—Cr matrix [1,2]. Its advantages are excellent corrosion and fatigue resistance in harsh environments or at elevated temperatures, as well as good weldability [3,4]. These superior thermochemical, mechanical and tribological properties make it favourable for applications in aerospace, marine, petrochemistry and nuclear. However, its high hardness and high work-hardening rate are reflected in a poor workability, which is the reason for its limited use in applications where complex geometries are required [1,5,6]. It is for this reason that nickel-based alloys, especially IN625 and IN718, are appropriate for additive manufacturing (AM) [7–10], where the demands of geometrical complexity and freedom of design can easily be achieved.

Laser powder-bed fusion (LPBF) is an attractive AM approach for metal parts with geometrical complexity. It is also the most studied AM process for IN625 components in a diverse range of applications. The LPBF parameters affect the resulting microstructure and the mechanical properties of the parts. Studies were conducted to investigate the variables (laser power, scan speed, hatch spacing, layer thickness, etc.) to obtain not only the desired macroscopic characteristics, but also the right density, grain size, orientation, melt-pool dimensions, etc. [11–14]. An overview of LPBF-processed IN625 was published by Tian et al. [15], focusing on the main material characteristics, such as microstructure evolution, the formation of defects (balling, porosity, cracks), the accumulation of residual stresses and mechanical properties. Further investigations [12,16–19] proved that a post-heat-treatment process is often necessary to eliminate (or at least reduce)

---

* Corresponding author.
E-mail address: matjaz.godec@imt.si (M. Godec).

https://doi.org/10.1016/j.surfcoat.2022.129130
Received 2 November 2022; Received in revised form 29 November 2022; Accepted 30 November 2022
Available online 7 December 2022

the residual stresses, the non-equilibrium phase and the micro-cracks present in the as-built LPBF parts. Four post-heat-treatment processes were reported for the LPBF of IN625: stress-relief annealing, recrystallisation annealing, solution treatment and hot isostatic pressing [16,17]. In general, high-temperature annealing (above 1000 °C) is beneficial to the recrystallisation and stress relief, while at temperatures below 1000 °C no obvious changes are detected [18]. To control the microstructure's evolution and the relief of the residual stress, the heat-treatment parameters (temperature and time) must be adapted to the needs of the individual application. However, such studies are rare.

One of the disadvantages of Ni-based alloys that limits their application is their poor tribological performance, i.e., low wear resistance, low surface hardness and high coefficient of friction [20–22]. To eliminate this, different surface-engineering techniques can be used to improve the surface properties. Conventional Ni-based alloys can be treated with different thermochemical processes, such as PVD [23], CVD [24], thermal spraying [25] and plasma nitriding [26,27]. A commonly used technique is pulsed-plasma-ion nitriding, where the nitrogen diffuses into the alloy, reacts with alloying elements and forms their nitrides. This leads to a hardened nitride layer on the surface of the alloy. Plasma nitriding is well-known and investigated for Fe-based alloys, but the nitriding of Ni-based alloys containing nitride-forming elements has received much less attention.

Pedraza et al. [28] reported that the nitride layer formed on Ni-based alloys is thinner than the ones formed on Fe-based alloys during plasma nitriding. A comprehensive investigation of plasma nitriding, including a wide range of nitriding parameters (nitriding temperatures from 550 to 750 °C, times from 1 to 16 h, different N_2:H_2 gas mixtures) was carried out by Aw et al. [29] for the Ni-based alloy IN718. They found that the time and temperature were not effective in increasing the thickness of the nitride layer. Kumar et al. [30] further characterised the low-temperature plasma nitriding of Inconel 600 and 601. They reported the formation of the epsilon (ε) and fcc (γ) phases for temperatures up to 450 °C, while the chromium nitride (CrN) phase was detected in the temperature range ~450 °C in the Inconel 601 alloy. Leroy et al. [31] applied low-temperature plasma nitriding to Inconel 690. Depending on the plasma reactivity, they observed two or three different metastable fcc nitrogen solid solutions that they referred to as γ_{N1}, γ_{N2} and γ_{N3}. The investigation by Borowski et al. [21] showed that the nitride layer formed after the plasma nitriding of IN625 was composed of chromium nitride (CrN) with a face-centred cubic structure and an orthorhombic structure, as well as γ_N formed beneath the CrN layer. The microstructural evolution (the formation of different phases and nitrides) in the nitride layer and the dependence of its nitriding temperature are not well understood and require further investigation.

The innovative approach of using plasma nitriding on different AM materials, such as stainless steel AISI 316 L [32], maraging steel 18Ni-300 [33–35] and Inconel 718 [36], was recently published by several authors. Although these investigations highlighted some promising results, they also raised several issues, which require careful investigations and explanations. Firstly, it is necessary to find the optimum nitriding parameters for specific AM alloys, which tend not to be the same as the nitriding parameters of the conventional manufactured (CM) alloys. The necessity and impact of any previous heat treatments on the nitriding process must be taken into account as well. With a knowledge of the nitriding kinetics, it is possible to tailor the formation of the nitride layer and the nitrides that are responsible for the tribological and corrosion properties of the surface.

This paper deals with the plasma nitriding of AM IN625 at two different temperatures (430 °C and 500 °C) on as-built and prior-heat-treated samples. As a comparison, samples of CM IN625 were plasma nitrided under the same conditions. The aim was to observe the differences in the nitriding kinetics due to the different initial conditions prior to the nitriding, the different nitriding temperatures and their influence on the specific surface properties, such as hardness, wear and corrosion resistance. The use of advanced analytical techniques provided us with an in-depth understanding of the microstructural features in the nitride layers. The conclusions are drawn on the basis of a comparison between the as-built, directly nitrided and the prior-heat-treated samples as well as from a comparison between the AM and CM materials.

2. Materials and methods

2.1. Materials

Gas-atomised powder from EOS GmbH (Germany) was used for the LPBF of cubic IN625 samples with dimensions of 30 × 30 × 30 mm^3. The size of the powder particles was 45 ± 15 μm. The samples were built using an industrial EOSINT M280 machine, equipped with a 400-watt fibre laser. The commercial LPBF process parameters were used: the laser power of 300 W, the laser diameter of 0.11 mm, the laser speed of 990 mm/s, the distance between the laser paths of 10 mm, the overlapping between laser paths of 0.08 mm. As a comparison, samples of IN625 manufactured using a conventional processing route were used. The chemical compositions of the additive manufactured (AM) and conventional manufactured (CM) samples are presented in Table 1.

2.2. Heat treatment

The LPBF as-built IN625 samples were subjected to two different heat-treatment conditions in an Ar atmosphere:

a) stress-relief (SR) annealing was carried out at 870 °C for 1 h
b) solutioning (ST) at 1050 °C for 1 h.

The initial condition for the CM IN625 is generally taken to be the condition after solution treatment. Therefore, the investigated reference CM samples were only solution treated at 1050 °C for 1 h. After the heat treatment all the samples were water quenched to suppress the microstructure evolution during cooling.

2.3. Plasma nitriding

Prior to the plasma nitriding, the samples were surface ground and mirror polished to ensure the intact appearance of the materials' surfaces and to remove any surface irregularities. The as-built LPBF samples, heat-treated (SR and ST) LPBF samples and the conventional reference samples were all plasma nitrided in a Metaplas Ionon HZIW 600/1000 cold-wall reactor in 75 vol% H_2: 25 vol% N_2 gas mixture at two nitriding temperatures N1 = 430 °C and N2 = 500 °C for 15 h. Nitriding of IN625 requires a relatively long nitriding duration to obtain a few μm thick nitride layer. All the investigated samples with their labels and conditions are listed in Table 2.

2.4. Microstructural characterisation

The microstructures were characterised on cross-sectioned samples prepared using standard metallographic procedures, which included mounting in conductive Bakelite resin, grinding and polishing. The samples were etched in Kroll's etchant (3 mL HF, 14 mL HNO_3, 83 mL H_2O).

The microstructural observations were carried out using a Nikon Microphot FXA optical microscope with an Olympus DP73 digital camera. Secondary-electron imaging (SEI), energy-dispersive spectroscopy (EDS) and electron-backscatter diffraction (EBSD) were performed on a Zeiss CrossBeam 550 field-emission scanning electron microscope (FE-SEM), with an EDAX Hikari Super EBSD camera using APEX software and EBSD post-processing using OIM 8.6 software. The parameters used for the SE images and the EDS analyses were a 15-kV accelerating voltage and a 2.0–5.0 nA probe current, while the EBSD analyses were performed on 70°-tilted samples and a 10-nA probe current. Electron channelling contrast imaging (ECCI) is an imaging technique performed

Table 1
Chemical composition of investigated IN625 samples in wt%.

	C	Si	Mn	S	Cr	Mo	Nb	Fe	Ti	P	Ni
AM IN625	0.010	0.35	0.037	0.004	20.5	8.8	3.8	0.78	0.36	<0.01	Bal
CM IN625	0.009	0.34	0.047	0.002	21.2	8.1	3.2	5.0	0.13	<0.01	Bal

Table 2
Sample labels and their condition.

Label	Sample condition
AM	LPBF as-built
AM+N1	LPBF as-built + nitrided at 430 °C/15 h
AM+N2	LPBF as-built + nitrided at 500 °C/15 h
AM+SR	LPBF as-built + annealed 870 °C/1 h
AM+SR + N1	LPBF as-built + annealed 870 °C/1 h + nitrided at 430 °C/15 h
AM+SR + N2	LPBF as-built + annealed 870 °C/1 h + nitrided at 500 °C/15 h
AM+ST	LPBF as-built + solution treated 1050 °C/1 h
AM+ST + N1	LPBF as-built + solution treated 1050 °C/1 h + nitrided at 430 °C/15 h
AM+ST + N2	LPBF as-built + solution treated 1050 °C/1 h + nitrided at 500 °C/15 h
CM + ST	Conventional manufactured + solution treated 1050 °C/1 h
CM + ST + N1	Conventional manufactured + solution treated 1050 °C/1 h + nitrided at 430 °C/15 h
CM + ST + N2	Conventional manufactured + solution treated 1050 °C/1 h + nitrided at 500 °C/15 h

in scanning electron microscopy using a backscatter detector. It is based on the electron-channelling effect, and the image is obtained from scattered electrons at crystal lattice defects. The ECCI was performed at an accelerating voltage of 25 kV and a current probe of 2 nA. X-ray Diffraction (XRD) was used to determine the phase composition. It was performed on a Panalyitical X'PERT Pro PW 3040/60 goniometer with Bragg-Brentano geometry (2Θ goniometer 30°–90°, a step size of 0.002° and a scan step time of 50 s per step). A Cu anode ($K_\alpha = 0.154$ nm) was employed with a 40-mA current and a potential of 45 kV.

2.5. Wear tests and hardness measurements

The tribological properties, including the wear volume and coefficient of friction, were determined from reciprocating, dry-sliding wear tests performed under standard room conditions ($T = 20$ °C, RH = 50 %). The tests were carried out on a tribometer with the ball-on-disc contact geometry, and a 20-mm-diameter 100Cr6 hardened bearing steel ball (58–60 HRC) used as the oscillating counter-body. The test parameters were as follows: a normal load of 28 N (corresponding to a nominal contact pressure of 900 MPa), an oscillating amplitude of 4 mm and frequency of 15 Hz, an average sliding speed of 0.12 m/s, a testing time of 833 s and a total sliding distance of 100 m. Three parallel tests were made on each sample listed in Table 2.

The wear tracks and wear volumes were analysed using an Alicona InfiniteFocus G4 3D high-resolution 3D confocal focus variation microscope.

The hardness was measured with an Instron Tukon 2100 B Vickers hardness tester (HV0.01) and an Instron B2000 Rockwell hardness tester (HRC). Nano-indentation measurements were carried out with Anton Paar's instrumented indentation tester Step 700 NHT3, designed for precise determinations of the mechanical properties of thin films or coatings, such as hardness and elastic modulus. The tests were performed on polished cross-section samples to detect the actual surface hardness. The applied load was 3 mN on the indentation matrix of 4 × 8 and with a 2-μm spacing between the indents. The instrumented hardness (HIT) and the instrumented elastic modulus (EIT) were calculated in a single rapid measurement.

2.6. Electrochemical measurements

Potentiodynamic curves were recorded in a 3.5 % NaCl solution at room temperature using a BioLogic® SP-300 Model Potentiostat/Galvanostat/FRA and EC-Lab® V11.27 software. The three-electrode electrochemical cell was applied with the investigated sample as a working electrode, a saturated calomel electrode as a reference electrode (−SCE, 0.242 V vs. SHE) and a platinum-mesh as a counter electrode. The samples were stabilised at the open-circuit potential for 1 h prior to the experiment, and the measurements were repeated three times to obtain statistically relevant results.

3. Results and discussion

The bulk microstructures observed using SEM and EBSD of the as-built (AM), as-built and heat-treated AM samples (AM+SR, AM+ST), as well as the conventional sample (CM + ST), are presented in Fig. 1. The as-built AM sample has a typical cellular structure with slightly columnar grains in the build direction (Fig. 1a). The shape of the grains after the stress-relief annealing at 870 °C (AM+SR) remained unchanged (Fig. 1b), while after solutioning (AM+ST) at 1050 °C, partial recrystallisation was observed (Fig. 1c). Some regions have a recrystallised structure, while others are just partially or even not recrystallised (left- and right-hand insets in Fig. 1c, respectively). The heat treatment at 870 °C causes the formation of fine precipitates in the form of short needles of δ-phase observed along nano dendrites and grain boundaries. The higher annealing temperature of 1050 °C caused the dissolution of the δ-precipitates. The conventional sample also solution heat treated (CM + ST) at 1050 °C was completely recrystallised (Fig. 1d). The conventional sample had some minor segregations, which resulted in the formation of some Laves phase [37].

Plasma nitriding led to the formation of a continuous, uniform, thick nitride layer. The observations show that the prior heat treatment affected the visual appearance of the nitride layer, which was slightly thinner. Fig. 2 compares the nitride layers of the AM and CM + ST samples for two different nitriding temperatures: N1 (430 °C) and N2 (500 °C). For all the samples, the nitride layers formed at 430 °C appeared as a single layer (Fig. 2a–d), while the nitride layers formed at 500 °C consisted of two layers (Fig. 2e–h). The nitride layer for the lower nitriding temperature consisted of a darker-grey area located in the upper part of the layer and a lighter-grey area on the bottom, which were not discretely separated. However, for the higher nitriding temperature the layer consists of two homogeneous layers, darker grey on the top and lighter grey on the bottom. The cellular structure remains visible in both the AM nitride layers, which are thicker than those of the CM + ST samples. The thickness of the nitride layers for sample AM+N1 was 4.9–6.9 μm, while for samples CM + ST + N1, AM+SR + N1 and AM+ST + N1, it ranges between 4.5 and 5.5 μm. The difference in thickness between the AM and CM + ST samples is related to the specific AM microstructure, characterised by a higher dislocation density, internal stresses and nanodendrite/cellular structure. During the heat treatment of the AM samples, the cellular structure disappears, the diffusion is decreased, and as a result thinner nitride layers are formed (Fig. 2c, d, g, h). The thickness of the nitride layers on the sample AM+N2 is 6.0–7.8 μm and they are thicker than for samples CM + ST + N2, AM+SR + N2 and AM+ST + N2, where the thickness is 5.7–6.7 μm. In general, thicker nitride layers are obtained at the higher nitriding temperature as well as for AM samples without any prior heat treatments. The thicknesses of all investigated nitrided layers are collected in

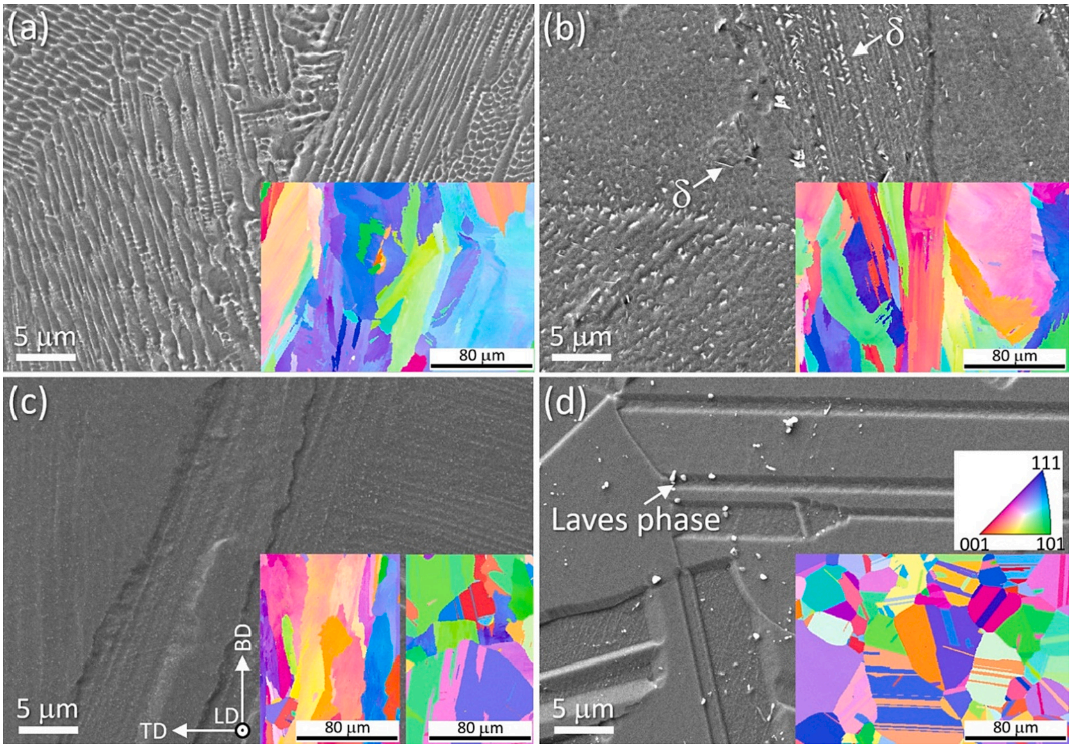

Fig. 1. SE images and the insets of EBSD IPF maps in the Z direction of samples: (a) AM, (b) AM+SR, (c) AM+ST and (d) CM + ST. The LD, TD and BD represent longitudinal, transverse and build direction, respectively.

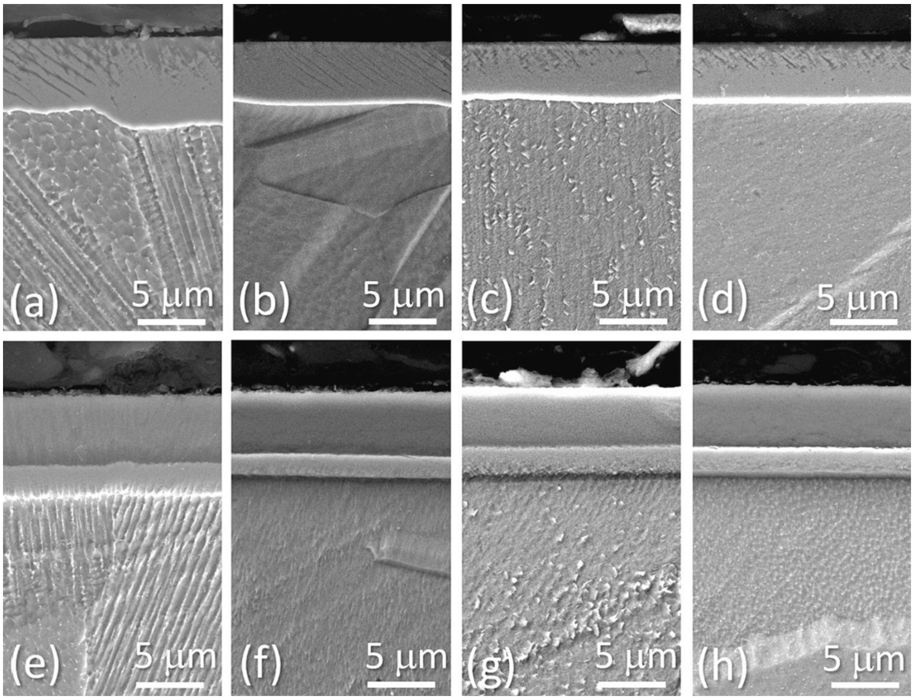

Fig. 2. SE images of nitride layers in cross-section of samples: (a) AM+N1, (b) CM + ST + N1, (c) AM+SR + N1, (d) AM+ST + N1, (e) AM+N2, (f) CM + ST + N2, (g) AM+SR + N2, (h) AM+ST + N2.

Table 3, measured on etched samples in SEM on at least ten locations through the sample (20 mm cross-section length).

From Fig. 3a it is evident that the thickness of the nitride layer changes slightly due to the different grain orientations. At the higher nitriding temperature this orientation dependence of the growth is less pronounced (Fig. 3d). The morphology of the nitride layers obtained by ECCI on the AM+N1 and AM+N2 samples is a step forward in the characterisation of the nitride layers' evolution. Based on ECCI images it is obvious that the nitride layers consist of a surface layer on the top and a diffusion layer beneath (the area between the dashed lines in Fig. 3a, d). The difference in the nitride layer's thickness correlates with the grain orientation and particularly with the cellular structure's

Table 3
Thicknesses of nitride layers for all investigated samples.

Sample	AM+N1	AM+N2	AM+SR + N1	AM+SR + N2	AM+ST + N1	AM+ST + N2	CM + ST + N1	CM + ST + N2
1 Thickness (μm)	5.9 ± 0.7	6.9 ± 0.7	5.1 ± 0.4	6.1 ± 0.4	5.0 ± 0.4	6.3 ± 0.4	5.2 ± 0.3	6.2 ± 0.3
2 Thickness (μm)	5.9 ± 0.7	4.6 ± 0.3	5.1 ± 0.4	4.2 ± 0.3	5.0 ± 0.4	4.2 ± 0.3	5.2 ± 0.3	4.2 ± 0.2
3 Thickness (μm)	–	2.3 ± 0.3	–	2.0 ± 0.2	–	2.1 ± 0.1	–	1.9 ± 0.1

1 - whole layer, 2 – upper layer, 3 – bottom layer

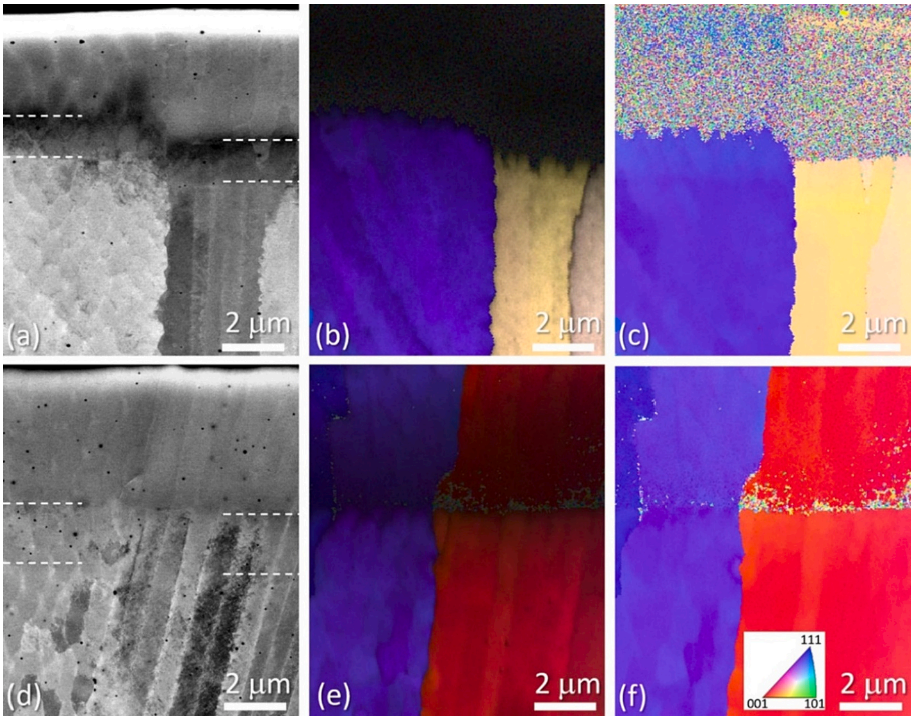

Fig. 3. ECCI images of cross-sections of samples (a) AM+N1 and (d) AM+N2 and the corresponding EBSD band-contrast image overlaid with the IPF Z orientation-coloured grain map (b) and (e), and EBSD IPF Z orientation-coloured grain maps (c) and (f).

orientation. Regions with cells or nanotubes oriented towards the nitrogen diffusion have the highest nitride-layer growth (right-hand area in Fig. 3a, d), while the cells or nanotubes oriented perpendicular (left-hand area in Fig. 3a, d) to the nitrogen diffusion have thinner nitrogen layers. This phenomenon is more noticeable at the lower nitriding temperature. In the microstructure of the AM samples, a lot of nanosized oxides were observed, originating from the thin oxide layer on each powder particle [38]. The orientation dependence is also determined by the EBSD maps for nitriding temperatures N1 (Fig. 3b, c) and N2 (Fig. 3e, f). Fig. 3b and e are EBSD band-contrast images overlaid with IPF Z orientation coloured grain maps. The sum of the detected peaks in the Hough Transform defines band contrast, and can describe the quality of an electron backscatter diffraction pattern. The darker colour corresponds to the weaker (blurred) Kikuchi patterns, which means that the nitride layer obtained at the lower temperature (Fig. 3b) is not indexing (or wrongly indexing) and IPF Z is observed as mixed-colour dots (Fig. 3c). This can be explained by the high concentration of nitrogen in the expanded austenite crystal lattice causing a lot of stress. At the higher nitriding temperature, the relaxation of the expanded austenite occurs due to CrN precipitation (determined later by XRD). The size of the CrN precipitates is too small to be detected by the EBSD; therefore, the EBSD analyses detect only the austenite phase (Fig. 3e, f). At the bottom of the nitride layer, the band contrast is weaker (darker areas in Fig. 3e), and some non-indexed area is observed (mixed-colour dots). The reason can be a reduced relaxation of the crystal lattice at the bottom of the nitride layer; however, the possibility of a step formation at the border of the nitride and diffusion layers, due to the sample's preparation cannot be excluded.

In the nitride layer obtained at the lower temperature, many slip lines were observed (Figs. 2a–d and 3a), formed due to the deformation of the fcc austenite structure and the generation of stacking faults and dislocations. A similar observation was reported by Leroy et al. [31] for a CM Ni-based alloy.

The XRD patterns of all the investigated samples are shown in Fig. 4. The peaks in the spectra of the AM and CM + ST samples before nitriding correlate well with the Ni-austenite (γ phase). The intensity of the (111) peak of the non-textured nickel alloy is the largest, seen on the CM + ST sample. Due to the specific orientation of the AM sample, the intensity of the (111) and (200) are exchanged. All the nitrided samples' spectra exhibit peaks corresponding to the γ phase. The intermetallic precipitates such as γ′ ($Ni_3(Al,Ti)$) and γ′′ (Ni_3Nb) have similar lattice parameters to the γ phase and are therefore in the same position in the XRD spectra. The XRD spectra for nitriding at the N1 and N2 temperatures are different [39–41]. On the spectra of N1 and N2, intensive peaks of γ phase are observed and at the higher temperature they are split to two peaks. The literature [36,41] reports for IN718 at higher nitriding temperatures a shift and broadening of the γ-peak to higher angles. From the XRD spectra, besides γ-peak also a new broad peak can be observed. The plasma nitriding of austenitic steels is known for the formation of expanded austenite (γ_N) at lower nitriding temperatures (up to 400–430 °C). The diffusion of nitrogen atoms at the interstitial positions causes supersaturations and expansion of the austenitic crystal lattice. At a higher nitriding temperature, the expanded austenite transforms into nitrides [31,32,41]. Tao et al. [41] reported the expanded austenite

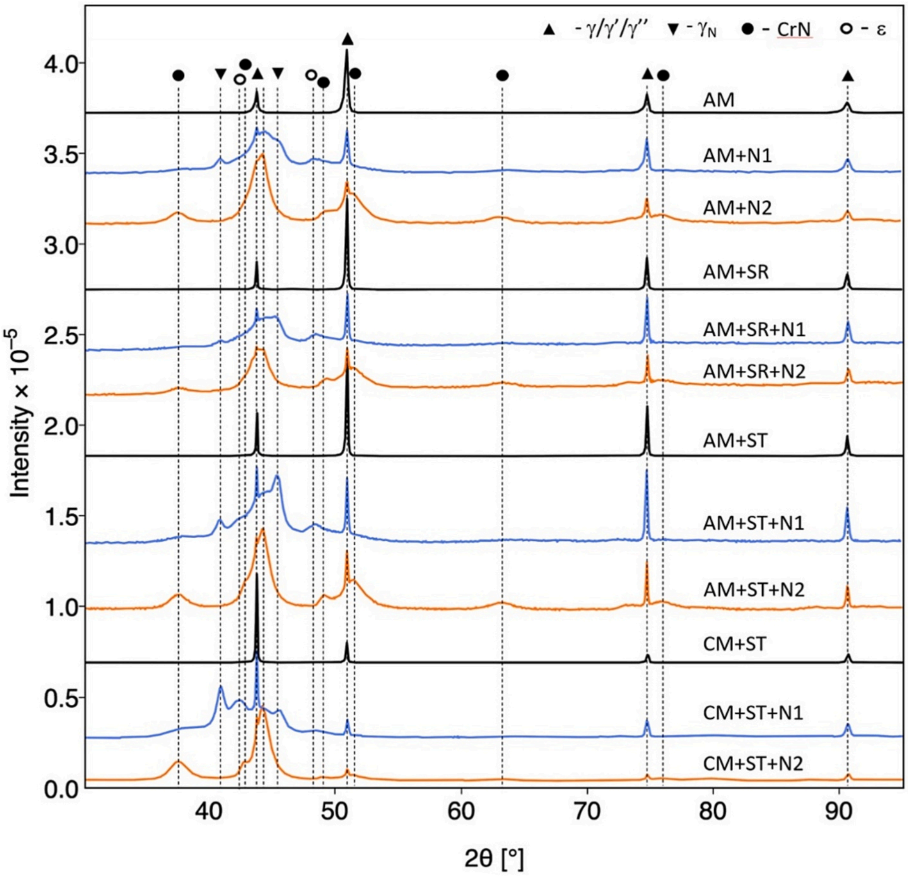

Fig. 4. XRD spectra of all the investigated samples.

peaks γ_N (111) and γ_N (200) at a similar position as obtained in this work ($2\theta = 40.9°$ and $45.5°$). The spectra obtained at the higher nitriding temperature (N2) have several CrN peaks, also reported by several authors [20,22,41,42]. The same peaks were also observed at lower nitriding temperatures, although with lower intensity. For the solution-treated (ST) samples the observed peaks are less broadened. Broadened peaks are, in general, obtained for nano-sized phases. Sharma et al. [20] mentioned very fine CrN formation on the surface, with sizes of 5–10 nm on IN690 after 4 h of nitriding at 350–450 °C. The intensities of some CrN peaks are different for the CM + ST and AM samples due to the growth orientation. The lower nitriding temperature N1 can cause the formation of ε-phase [20,30,42], defined as Ni_3N or $(Ni, Cr, Fe, Mn)_3N_{1-x}$.

The EDS line scans and the EDS maps were measured on AM samples for both nitriding temperatures (Fig. 5). They clearly showed the presence of two layers in both cases, by revealing the diffusion layer beneath the top layer. The diffusion layer obtained at the lower temperature was approximately 20–40 % thinner than the diffusion layer obtained at the higher temperature. A very similar thickness ratio was obtained for the surface layer. On the very surface (<1 μm), a significant increase in nitrogen was observed for both samples, and then the nitrogen curve at the line scan shows a type of plateau, which correlates with the thickness of the top nitride layer. The amount of nitrogen decreases through the diffusion layer, correlating well with the depth of the diffusion layers in Fig. 3a, d. The SEM analyses show that chemical etching (Kroll etchant) of the samples at the lower nitriding temperature does not reveal any diffusion layer (Fig. 2a–d), while at the higher nitriding temperature the diffusion layer is shown as a very discrete layer (Fig. 2e–h). The reason for the different behaviour of the diffusion layers to the chemical etchant might be the result of the slightly different chemical composition or the presence of precipitates. It is known [43–45] that Inconel alloys tend to form nano segregations. Elements such as Nb, Mo and Ti segregate on the cellular borders (higher dislocation density), while the inner cell areas are enriched with Ni, Cr and Fe [43]. Nano segregations could explain the scattering of line scans of the elements, and the distance of the individual peaks is at the same level as the size of the cells. The enrichment of Mo and Nb correlates with the depletion of Ni and Cr.

The microhardness measurements (Vickers HV0.1) on the surface show a significant increase in the hardness after nitriding, particularly at the higher nitriding temperature, and such a trend is observed for all the samples, regardless of the previous heat treatment and method of manufacturing (Fig. 6a). The highest hardness before nitriding is observed for the AM sample, due to high internal stresses, cellular structure and high dislocation density. The treatment for stress relief causes a slight drop in hardness due to the decomposition of the cellular structure, which is compensated by the precipitation hardening. The lowest hardness of the AM samples is obtained after solution treatment, with the absence of cellular structure and precipitates. The hardness of the CM + ST samples is even lower. Nitriding significantly increases the surface hardness 2–3 times. At the lower nitriding temperature (N1) the hardness increase is caused by supersaturation of the austenite, also containing a very small amount of CrN (very weak peaks in the XRD spectra). The higher nitriding temperature (N2) leads to an even higher hardness, due to substantial CrN precipitation from the supersaturated austenite phase. The solution-treated samples do not exhibit such a difference in hardness for the two nitriding temperatures. The reasons are the lower hardness of the substrate, which lead to a softer nitride layer, and the influence of the substrate's contribution to the measurements due to the very thin layer. The smaller values of the hardness obtained for the solution-treated AM+ST and CM + ST samples can be attributed to there being less nano segregation of Cr, and so less CrN precipitation occurs.

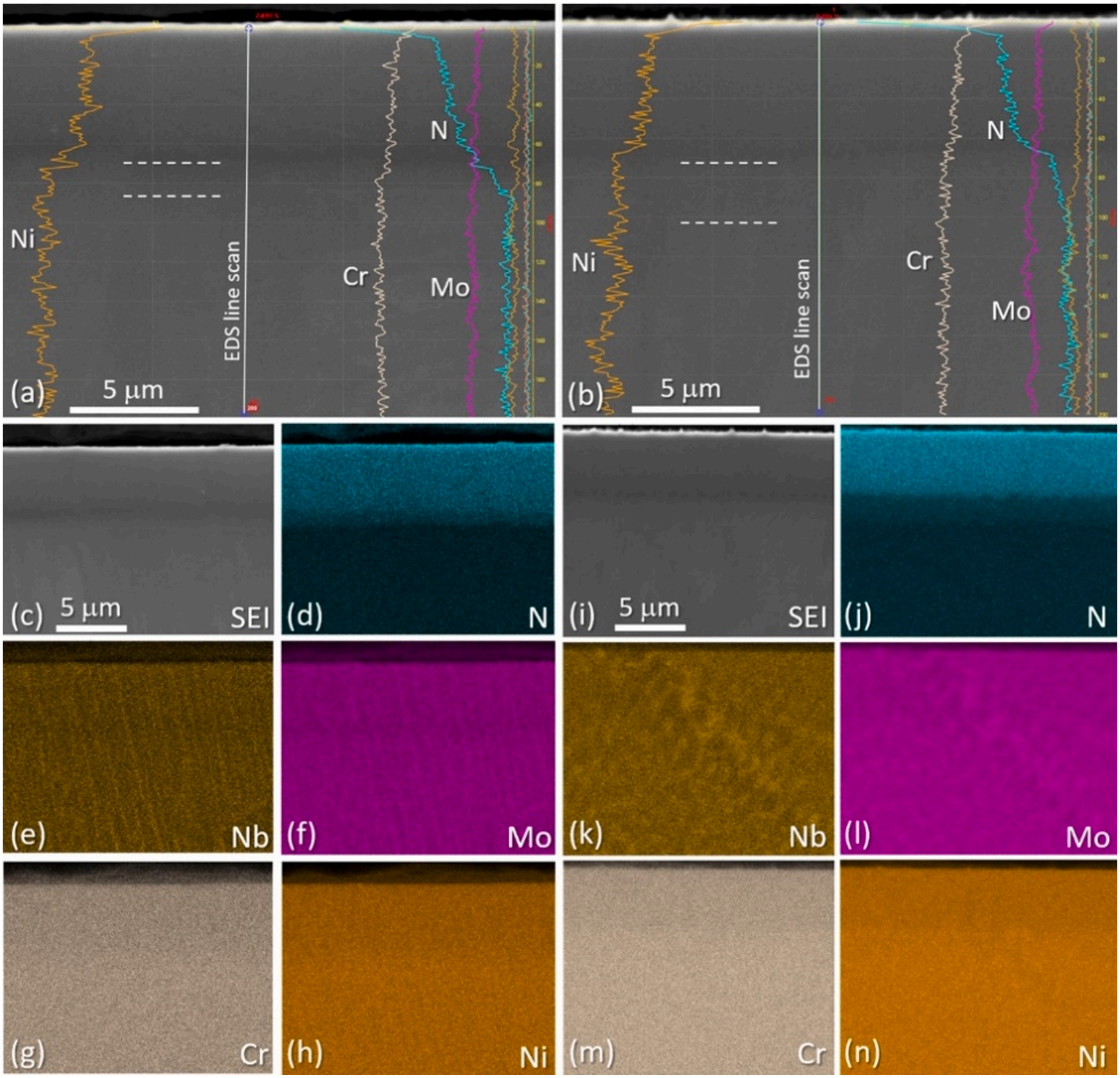

Fig. 5. EDS line profile on SE images of (a) AM+N1 and (b) AM+N2. The nitride layers are marked with a dashed white line. Panels (c)–(h) and Panels (i)–(n) represent the corresponding EDS maps for AM+N1 and AM+N2, respectively.

Nano-indentation measurements performed in the middle of the top nitride layer, in the middle of the diffusion layer and in the substrate for both AM+N1 and AM+N2 samples are presented in Fig. 6b. The hardness (Fig. 6b) of the substrates is almost identical. The slight increase for sample AM+N2 can be attributed to the higher nitriding temperature, causing the precipitates to start forming. Interestingly, the diffusion layer's hardness is higher at the lower nitriding temperature, and the opposite occurs in the top layer. This difference in hardness also indicates that the diffusion layers are chemically or microstructural revealed by different chemical etchants, as previously discussed. The higher nitriding temperature results in the hardest top layer. The lower nitriding temperature causes the formation of a diffusion layer of 11.9 GPa (equivalent to about 1210 HV) and a top layer of 14.4 GPa (equivalent to about 1470 HV), while the higher nitriding temperature causes the formation of a diffusion layer of 9.9 GPa (equivalent to about 1010 HV) and a top layer of 18.6 GPa (equivalent to about 1900 HV). Fig. 6c shows the elastic modulus of all the layers and substrates. The hardest top layer of nitride layer obtained at the higher nitriding temperature also has the highest elastic modulus.

For all the investigated samples the main wear mechanism was adhesive wear combined with abrasive wear (Fig. 7), with plasma nitriding significantly reducing the abrasive part, as shown in Fig. 8a. The steady-state coefficient of friction (average value for the last 750 s/90 m of sliding) was in the range 0.66–0.68 for the as-built samples (Fig. 8b). Heat treatment of the AM samples (stress-relieving and solutioning) leads to a slight drop in friction; however, the values remain above 0.6. With plasma nitriding the steady-state coefficient of friction is further reduced below 0.6 for the lower nitriding temperature (N1) and even down to 0.4 for the higher nitriding temperature (N2), related to the higher surface hardness and the reduced abrasive-wear component.

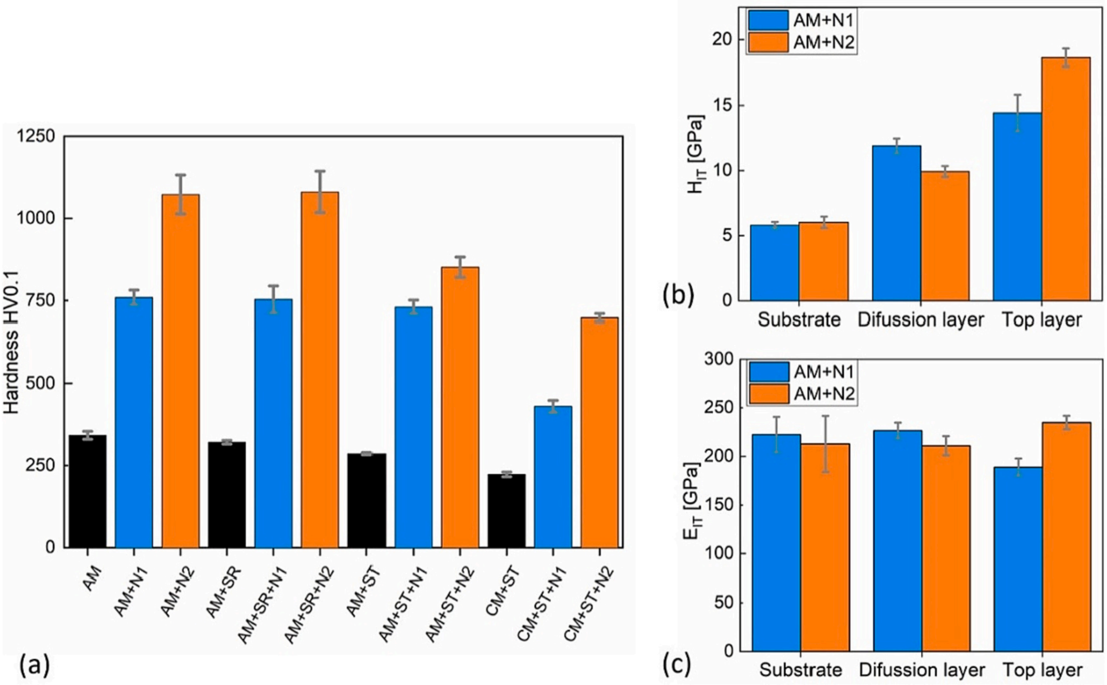

Fig. 6. (a) Surface-hardness measurements HV0.1 for all the investigated samples, (b) nano-indentation measurements H_{IT}, and (c) elastic modulus E_{IT} for AM+N1 and AM+N2 samples.

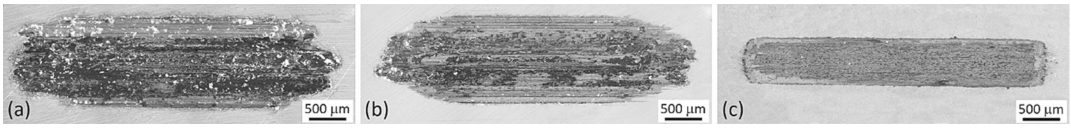

Fig. 7. Typical wear scars for IN625 samples: (a) CM + ST, (b) AM and (c) AM+N2.

With an increase in hardness, surface becomes more resistant to scratching, microcuting and especially ploughing caused by the counter-body asperities, which in turn reduces sliding resistance and coefficient of friction. Harder surfaces may also show reduced adhesive friction component attributed to the greater strength of the interatomic bonds and the high surface energy [46]. For both nitriding temperatures the CM has a 5–10 % lower steady-state friction.

In terms of wear rate (Fig. 8a), for the as-built AM material the abrasive-wear rate component (material removed from the sample surface) after 100 m of sliding against the hardened 100Cr6 ball was $1.5 \cdot 10^{-5}$ mm^3/Nm and the adhesive wear component (material adhered to the sample surface) $1.5 \cdot 10^{-6}$ mm^3/Nm. The CM + ST, on the other hand, has similar abrasive and adhesive-wear rate components of about $7 \cdot 10^{-6}$ mm^3/Nm, mainly related to the lower hardness and the coarser microstructure, thus promoting adhesive wear relative to the as-built AM sample. Heat treatment of the AM material resulted in a reduced hardness and some microstructural changes, leading to an increased wear rate, especially the adhesive component, as shown in Fig. 8a. Plasma nitriding, on the other hand, through the nitride layer's formation and the increased surface hardness for all the samples, improved both the adhesive wear resistance (~40 %) and especially the abrasive wear resistance (by two orders of magnitude). The higher nitriding temperature (N2) provides slightly better results (10–20 %) for the AM material, but considerably more for the CM + ST material (40–50 %), related to a more significant difference in the surface hardnesses for the two nitriding conditions. On the other hand, no difference between the differently heat-treated and nitrided AM samples could be observed, due to the wear volume being concentrated within the nitride layer for all the samples.

The potentiodynamic behaviour of the investigated samples in a 3.5 % NaCl solution and the corresponding corrosion potentials (E_{corr}), corrosion-current densities (i_{corr}) and corrosion rates (v_{corr}) are presented in Fig. 9. The calculations of v_{corr} and i_{corr} were made according to ASTM G102 – 89 (2015) [47]. The results show that the heat treatment did not significantly influence the corrosion behaviour of the samples compared to the as-built AM sample. The range of passivation was similar for the as-built AM, the heat-treated AM as well as the heat-treated CM + ST samples. However, the i_{corr} and v_{corr} values slightly increased compared to the as-built AM sample. The polarisation and passivation behaviours of the tested materials were mainly affected by the plasma-nitriding temperatures. It appeared that early-stage nitride formation at the lower nitriding temperature slightly shifted the potentiodynamic curves to lower corrosion-current densities, indicating a slight improvement in the corrosion performance. On the other hand, the higher nitriding temperature caused a substantial decrease in the passivation region. Compared to the as-built AM sample, where a broad passivation range up to 0.7 V (SCE) was observed, in the case of all the samples treated at the higher nitriding temperature, it extends only up to 0.2 V (SCE), indicating poorer passivity. The reduced corrosion resistance can be attributed to the transformation of the expanded austenite, accompanied by the local depletion of Cr due to the formation of Cr_xN_y phases. The formation of Cr_xN_y phases is actually the precipitation of Cr-nitrides from the expanded austenite [41].

The nitriding of the alloys with austenite microstructure as stainless steels and Ni-based alloys is generally carried out at lower nitriding temperatures not exceeding 450 °C to prevent the formation of Cr nitrides known for their detrimental impact on corrosion. During nitriding, nitrogen atoms diffuse into the austenite, where they occupy

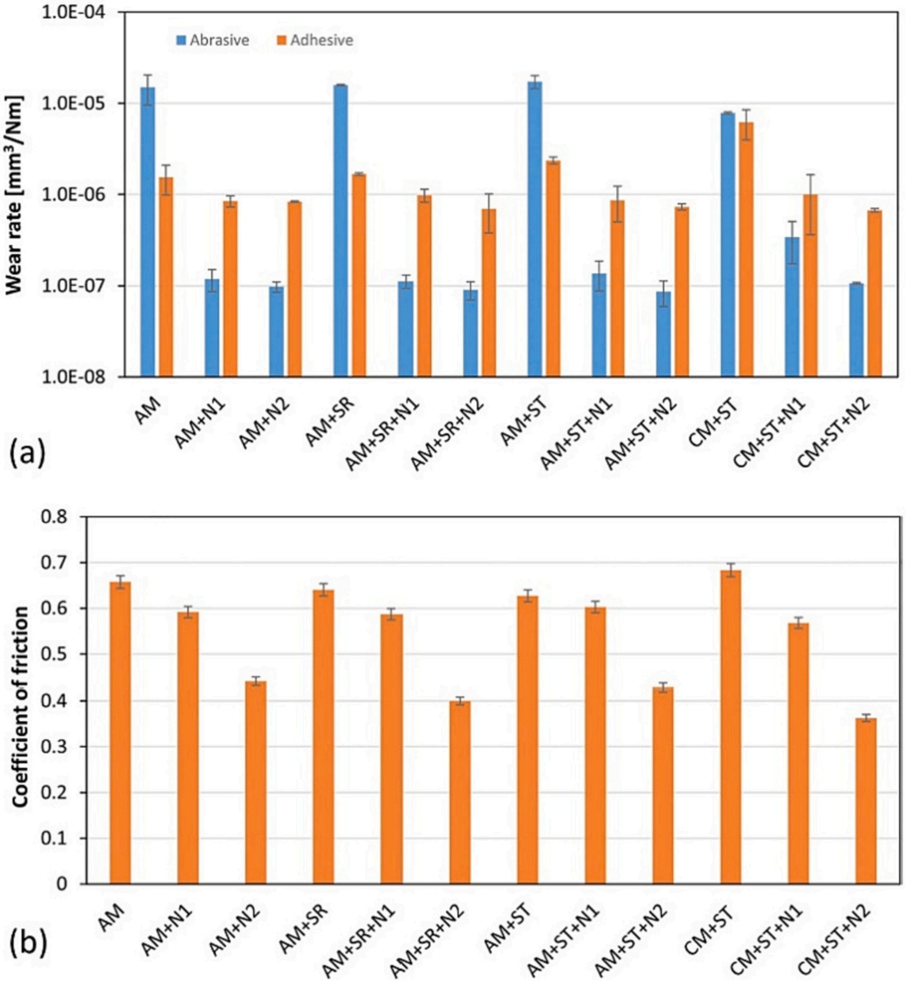

Fig. 8. (a) Wear volume and (b) steady-state coefficient of friction for all the investigated samples sliding against a hardened 100Cr6 ball.

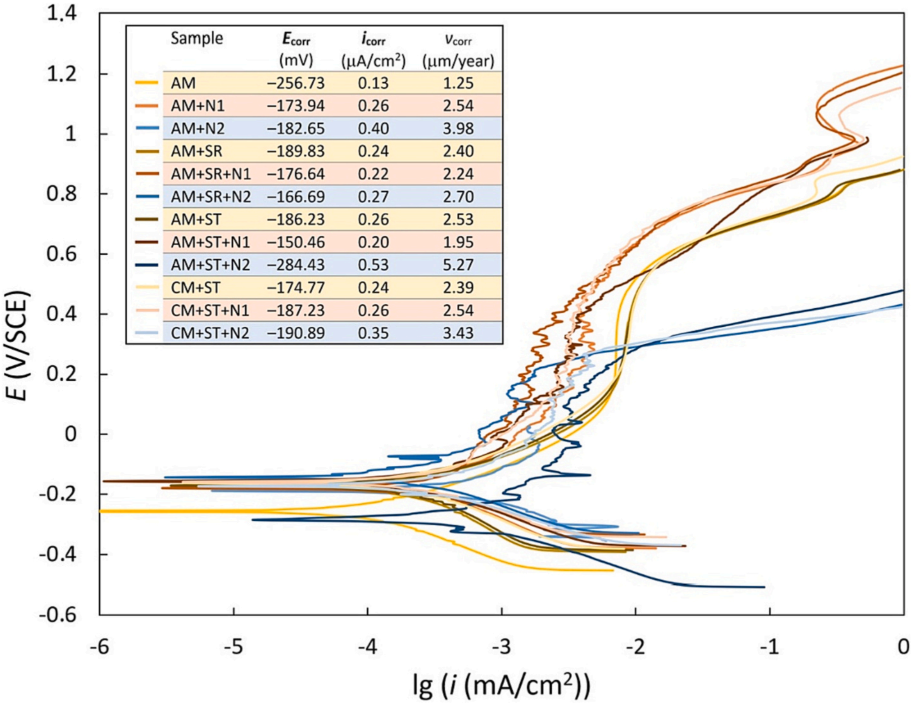

	Sample	E_{corr} (mV)	i_{corr} (μA/cm²)	v_{corr} (μm/year)
—	AM	−256.73	0.13	1.25
—	AM+N1	−173.94	0.26	2.54
—	AM+N2	−182.65	0.40	3.98
—	AM+SR	−189.83	0.24	2.40
—	AM+SR+N1	−176.64	0.22	2.24
—	AM+SR+N2	−166.69	0.27	2.70
—	AM+ST	−186.23	0.26	2.53
—	AM+ST+N1	−150.46	0.20	1.95
—	AM+ST+N2	−284.43	0.53	5.27
—	CM+ST	−174.77	0.24	2.39
—	CM+ST+N1	−187.23	0.26	2.54
—	CM+ST+N2	−190.89	0.35	3.43

Fig. 9. Electrochemical parameters calculated from potentiodynamic curves in a 3.5 % NaCl solution for all investigated samples.

interstitial positions, expand the crystal lattice of austenite and harden it. Higher nitriding temperatures cause the intensive precipitation of very fine Cr nitrides in the austenite matrix occurs most probably at a certain nitrogen concentration. On the other hand, the Kroll's etchant is most likely sensitive to certain Cr nitrides concentrations.

4. Conclusions

Plasma-assisted nitriding at two different temperatures (430 °C and 500 °C) was used to investigate the kinetics of the nitride layers' growth, the microstructural behaviour and the wear and corrosion resistance of an additive-manufactured (AM) IN625 in comparison with a conventional manufactured (CM) IN625. Based on the results, the following conclusions can be drawn:

- The plasma nitriding at temperatures of 430 °C and 500 °C for 15 h caused the formation of hard nitride layers on the surface that are morphologically different, depending on the temperature. The nitride layers on the AM samples were slightly thicker than on the CM samples.
- The growth kinetics of the nitride layers strongly depends on the manufacturing route, the prior heat treatment and the nitriding temperature. AM creates specific microstructures with high internal stresses and, particularly, a high concentration of crystal lattice defects, enabling a faster diffusion rate of the nitrogen. With prior heat treatments, the lattice defects and stresses are removed. Depending on the temperature, intermetallic precipitates can form or be dissolved.
- The nitride layer formed at 430 °C and was revealed by SE images to be a single layer, while at 500 °C, it seems to be composed of two layers. On the other hand, EDS analyses and ECCI images defined nitride layers for both nitriding temperatures, being composed of two layers (surface and diffusion layers) with different amounts of nitrogen.
- The lower nitriding temperature caused the formation of an expanded austenite or a combination of expanded austenite and CrN, determined by the XRD measurements. The higher nitriding temperature leads to the decomposition of the expanded austenite and to the formation/precipitation of CrN. Based on the microstructure characterisation it is clear that all the layers consist of a thicker surface layer and a thinner diffusion layer. At the lower nitriding temperature, the surface layer contains supersaturated austenite γ-phase with a very small number of CrN precipitates. The presence of slip lines indicates that there are high internal stresses in the layer. At the higher nitriding temperature, the extended precipitation of CrN occurs and leads to crystal lattice relaxation (i.e., the absence of slip lines).
- The wear resistance, especially abrasive component, obtained after plasma nitriding is significantly improved and does not depend substantially on the previous heat treatment and nitriding temperature.
- In terms of corrosion resistance, plasma nitriding should be carried out at the lower nitriding temperature, where the precipitation of CrN, responsible for the reduction of the corrosion performance, does not occur or is not as significant as at higher temperatures.

CRediT authorship contribution statement

Danijela Anica Skobir Balantič: Investigation, Writing- Original draft preparation, Writing - Review & Editing.

Bojan Podgornik: Investigation, Writing – Review & Editing.

Aleksandra Kocijan: Investigation, Writing - Review & Editing.

Črtomir Donik: Investigation.

Matjaž Godec: Conceptualization, Investigation, Supervision, Writing- Original draft preparation, Writing - Review & Editing.

Declaration of competing interest

We wish to confirm that there are no known conflicts of interest associated with this publication and there has been no significant financial support for this work that could have influenced its outcome.

We confirm that the manuscript has been read and approved by all named authors and that there are no other persons who satisfied the criteria for authorship but are not listed. We further confirm that the order of authors listed in the manuscript has been approved by all of us. We confirm that we have given due consideration to the protection of intellectual property associated with this work and that there are no impediments to publication, including the timing of publication, with respect to intellectual property. In so doing we confirm that we have followed the regulations of our institutions concerning intellectual property. We understand that the Corresponding Author is the sole contact for the Editorial process (including Editorial Manager and direct communications with the office). He/she is responsible for communicating with the other authors about progress, submissions of revisions and final approval of proofs. We confirm that we have provided a current, correct email address which is accessible by the Corresponding Author and which has been configured to accept email from matjaz.godec@imt.si

Authors:

D. A. Skobir Balantič, Č. Donik, B. Podgornik, A. Kocijan, M. Godec.

Data availability

Data will be made available on request.

Acknowledgments

This work was financially supported by the Slovenian Research Agency (Project No. L2-2613 and core funding Nos. P2-0132 and P2-0050). The authors would like to thank Mr. Matjaž Rejec from the company Anton Paar d.o.o. for providing/enabling the measurements with a nano-indentation tester on the Anton Paars' equipment. Thanks Dr. Vojteh Leskovšek for valuable discussions and ideas regarding plasma nitriding.

References

[1] J.A. Gonzalez, J. Mireles, S.W. Stafford, M.A. Perez, C.A. Terrazas, R.B. Wicker, Characterization of inconel 625 fabricated using powder-bed-based additive manufacturing technologies, J. Mater. Process. Technol. 264 (2019) 200–210, https://doi.org/10.1016/j.jmatprotec.2018.08.031.

[2] C.P. Paul, P. Ganesh, S.K. Mishra, P. Bhargava, J. Negi, A.K. Nath, Investigating laser rapid manufacturing for Inconel-625 components, Opt. Laser Technol. 39 (2007) 800–805, https://doi.org/10.1016/j.optlastec.2006.01.008.

[3] K.D. Ramkumar, W.S. Abraham, V. Viyash, N. Arivazhagan, A.M. Rabel, Investigations on the microstructure, tensile strength and high temperature corrosion behaviour of inconel 625 and inconel 718 dissimilar joints, J. Manuf. Process. 25 (2017) 306–322, https://doi.org/10.1016/j.jmapro.2016.12.018.

[4] Ö. Özgün, H. Özkan Gülsoy, R. Yilmaz, F. Findik, Injection molding of nickel based 625 superalloy: sintering, heat treatment, microstructure and mechanical properties, J. Alloys Compd. 546 (2013) 192–207, https://doi.org/10.1016/j.jallcom.2012.08.069.

[5] M. Tripathy, M. Munther, K. Davami, A. Beheshti, Surface property study of additively manufactured inconel 625 at room temperature and 510 °C, Manuf. Lett. 26 (2020) 69–73, https://doi.org/10.1016/j.mfglet.2020.10.001.

[6] Z. Wang, A.D. Stoica, D. Ma, A.M. Beese, Stress relaxation in a nickel-base superalloy at elevated temperatures with in situ neutron diffraction characterization: application to additive manufacturing, Mater. Sci. Eng. A 714 (2018) 75–83, https://doi.org/10.1016/j.msea.2017.12.058.

[7] N. Mohammadian, S. Turenne, V. Brailovski, Surface finish control of additively-manufactured inconel 625 components using combined chemical-abrasive flow polishing, J. Mater. Process. Technol. 252 (2018) 728–738, https://doi.org/10.1016/j.jmatprotec.2017.10.020.

[8] K.N. Amato, S.M. Gaytan, L.E. Murr, E. Martinez, P.W. Shindo, J. Hernandez, S. Collins, F. Medina, Microstructures and mechanical behavior of Inconel 718 fabricated by selective laser melting, Acta Mater. 60 (2012) 2229–2239, https://doi.org/10.1016/j.actamat.2011.12.032.

[9] Q. Jia, D. Gu, Selective laser melting additive manufacturing of inconel 718 superalloy parts: densification, microstructure and properties, J. Alloys Compd. 585 (2014) 713–721, https://doi.org/10.1016/j.jallcom.2013.09.171.

[10] V.A. Popovich, E.V. Borisov, A.A. Popovich, V.S. Sufiiarov, D.V. Masaylo, L. Alzina, Impact of heat treatment on mechanical behaviour of inconel 718 processed with tailored microstructure by selective laser melting, Mater. Des. 131 (2017) 12–22, https://doi.org/10.1016/j.matdes.2017.05.065.

[11] C. Li, Y.B. Guo, J.B. Zhao, Interfacial phenomena and characteristics between the deposited material and substrate in selective laser melting inconel 625, J. Mater. Process. Technol. 243 (2017) 269–281, https://doi.org/10.1016/j.jmatprotec.2016.12.033.

[12] C. Li, R. White, X.Y. Fang, M. Weaver, Y.B. Guo, Microstructure evolution characteristics of inconel 625 alloy from selective laser melting to heat treatment, Mater. Sci. Eng. A 705 (2017) 20–31, https://doi.org/10.1016/j.msea.2017.08.058.

[13] C. Qiu, H. Chen, Q. Liu, S. Yue, H. Wang, On the solidification behaviour and cracking origin of a nickel-based superalloy during selective laser melting, Mater. Charact. 148 (2019) 330–344, https://doi.org/10.1016/j.matchar.2018.12.032.

[14] L.N. Carter, X. Wang, N. Read, R. Khan, M. Aristizabal, K. Essa, M.M. Attallah, Process optimisation of selective laser melting using energy density model for nickel based superalloys, Mater. Sci. Technol. 32 (2016) 657–661, https://doi.org/10.1179/1743284715Y.0000000108.

[15] Z. Tian, C. Zhang, D. Wang, W. Liu, X. Fang, D. Wellmann, Y. Zhao, Y. Tian, A review on laser powder bed fusion of Inconel 625 nickel-based alloy, Appl. Sci. 10 (2020), https://doi.org/10.3390/app10010081.

[16] A. Kreitcberg, V. Brailovski, S. Turenne, Effect of heat treatment and hot isostatic pressing on the microstructure and mechanical properties of Inconel 625 alloy processed by laser powder bed fusion, Mater. Sci. Eng. A 689 (2017) 1–10, https://doi.org/10.1016/j.msea.2017.02.038.

[17] X.Y. Fang, H.Q. Li, M. Wang, C. Li, Y.B. Guo, Characterization of texture and grain boundary character distributions of selective laser melted Inconel 625 alloy, Mater. Charact. 143 (2018) 182–190, https://doi.org/10.1016/j.matchar.2018.02.008.

[18] G.P. Dinda, A.K. Dasgupta, J. Mazumder, Laser aided direct metal deposition of Inconel 625 superalloy: microstructural evolution and thermal stability, Mater. Sci. Eng. A 509 (2009) 98–104, https://doi.org/10.1016/j.msea.2009.01.009.

[19] S. Li, Q. Wei, Y. Shi, Z. Zhu, D. Zhang, Microstructure characteristics of Inconel 625 superalloy manufactured by selective laser melting, J. Mater. Sci. Technol. 31 (2015) 946–952, https://doi.org/10.1016/j.jmst.2014.09.020.

[20] Y. Sharma, R. Kumar, V. Vidyasagar, D. Bhardwaj, Low temperature plasma ion nitriding (PIN) of Inconel 690 alloy, Mater. Res. Express. 6 (2018), https://doi.org/10.1088/2053-1591/aaf1f3.

[21] T. Borowski, A. Brojanowska, M. Kost, H. Garbacz, T. Wierzchoń, Modifying the properties of the Inconel 625 nickel alloy by glow discharge assisted nitriding, Vacuum 83 (2009) 1489–1493, https://doi.org/10.1016/j.vacuum.2009.06.056.

[22] N. Espallargas, S. Mischler, Dry wear and tribocorrosion mechanisms of pulsed plasma nitrided Ni–Cr alloy, Wear 270 (2011) 464–471, https://doi.org/10.1016/j.wear.2010.12.008.

[23] F. Klocke, K. Gerschwiler, R. Fritsch, D. Lung, PVD-coated tools and native ester - an advanced system for environmentally friendly machining, Surf. Coat. Technol. 201 (2006) 4389–4394, https://doi.org/10.1016/j.surfcoat.2006.08.089.

[24] B. Ning, M.E. Stevenson, M.L. Weaver, R.C. Bradt, Apparent indentation size effect in a CVD aluminide coated Ni-base superalloy, Surf. Coat. Technol. 163 (2003) 112–117, https://doi.org/10.1016/S0257-8972(02)00604-7.

[25] A.H. Dent, A.J. Horlock, D.G. McCartney, S.J. Harris, Microstructural characterisation of a Ni-Cr-B-C based alloy coating produced by high velocity oxy-fuel thermal spraying, Surf. Coat. Technol. 139 (2001) 244–250, https://doi.org/10.1016/S0257-8972(01)00996-3.

[26] F. Kahraman, S. Karadeniz, Characterization and Wear behavior of plasma nitrided nickel based dental alloy, Plasma Chem. Plasma Process. 31 (2011) 595–604, https://doi.org/10.1007/s11090-011-9301-8.

[27] R. Kumar, Y.C. Sharma, V. Vidyasagar, D. Bhardwaj, Wear behavior of plasma nitrided Inconel 690 alloy, AIP Conf. Proc. 2115 (2019) 30282, https://doi.org/10.1063/1.5113121.

[28] F. Pedraza, M. Reffass, G. Abrasonis, C. Savall, J.P. Rivière, J.F. Dinhut, Low-energy high-flux nitriding of Ni and Ni20Cr substrates, Surf. Coat. Technol. 176 (2004) 236–242, https://doi.org/10.1016/S0257-8972(03)00735-7.

[29] P.K. Aw, A.W. Batchelor, N.L. Loh, Structure and tribological properties of plasma nitrided surface films on Inconel 718, Surf. Coat. Technol. 89 (1997) 70–76, https://doi.org/10.1016/S0257-8972(96)02937-4.

[30] R. Kumar, Y. Chandra Sharma, V. Vidya Sagar, D. Bhardwaj, Chsracterization of low temperature plasma ion nitriding (PIN) of Inconel 600 and 601 alloys, Iran. J. Mater. Sci. Eng. 17 (2020), https://doi.org/10.22068/ijmse.17.2.20.

[31] C. Leroy, T. Czerwiec, C. Gabet, T. Belmonte, H. Michel, Plasma assisted nitriding of Inconel 690, Surf. Coat. Technol. 142–144 (2001) 241–247, https://doi.org/10.1016/S0257-8972(01)01243-9.

[32] M. Godec, C. Donik, A. Kocijan, B. Podgornik, D.A.S. Balantic, Effect of post-treated low-temperature plasma nitriding on the wear and corrosion resistance of 316L stainless steel manufactured by laser powder-bed fusion, Addit. Manuf. 32 (2020), https://doi.org/10.1016/j.addma.2019.101000.

[33] M. Godec, B. Podgornik, A. Kocijan, Č. Donik, D.A.S. Balantič, Use of plasma nitriding to improve the wear and corrosion resistance of 18Ni-300 maraging steel manufactured by selective laser melting, Sci. Rep. 11 (2021) 3277, https://doi.org/10.1038/s41598-021-82572-y.

[34] M. Godec, F. Ruiz-Zepeda, B. Podgornik, Č. Donik, A. Kocijan, D.A. Skobir Balantič, The influence of the plasma-nitriding temperature on the microstructure evolution and surface properties of additive-manufactured 18Ni300 maraging steel, Surf. Coat. Technol. 433 (2022), 128089, https://doi.org/10.1016/j.surfcoat.2022.128089.

[35] Y. Hong, D.D. Dong, S.S. Lin, W. Wang, C.M. Tang, T.C. Kuang, M.J. Dai, Improving surface mechanical properties of the selective laser melted 18Ni300 maraging steel via plasma nitriding, Surf. Coat. Technol. 406 (2021), 126675, https://doi.org/10.1016/j.surfcoat.2020.126675.

[36] G.C. Mondragón-Rodríguez, N. Torres-Padilla, N. Camacho, D.G. Espinosa-Arbeláez, G.V. de León-Nope, J.M. González-Carmona, J.M. Alvarado-Orozco, Surface modification and tribological behavior of plasma nitrided inconel 718 manufactured via direct melting laser sintering method, Surf. Coat. Technol. 387 (2020), 125526, https://doi.org/10.1016/j.surfcoat.2020.125526.

[37] S. Malej, Razvoj mikrostrukture v deformirani nikljevi zlitini 625, Naravoslovnotehniška fakulteta. https://repozitorij.uni-lj.si/IzpisGradiva.php?lang=slv&id=111489, 2019. TT - Microstructure development in deformed nickel alloy 625.

[38] M. Godec, S. Zaefferer, B. Podgornik, M. Šinko, E. Tchernychova, Quantitative multiscale correlative microstructure analysis of additive manufacturing of stainless steel 316L processed by selective laser melting, Mater. Charact. 160 (2020), 110074, https://doi.org/10.1016/j.matchar.2019.110074.

[39] G. Bertrand, C. Savall, C. Meunier, Structural characterisation (AFM and XRD) and hardness of spultered CrxNy coatings, Surf. Eng. 14 (1998) 246–249, https://doi.org/10.1179/sur.1998.14.3.246.

[40] T.M. Project, Materials Data on CrN by Materials Project, 2020, https://doi.org/10.17188/1196741.

[41] X. Tao, J. Kavanagh, X. Li, H. Dong, A. Matthews, A. Leyland, An investigation of precipitation strengthened Inconel 718 superalloy after triode plasma nitriding, Surf. Coat. Technol. 442 (2022), 128401, https://doi.org/10.1016/j.surfcoat.2022.128401.

[42] Y. Sun, Kinetics of layer growth during plasma nitriding of nickel based alloy Inconel 600, J. Alloys Compd. 351 (2003) 241–247, https://doi.org/10.1016/S0925-8388(02)01034-4.

[43] M. Godec, S. Malej, D. Feizpour, Č. Donik, M. Balažic, D. Klobčar, L. Pambaguian, M. Conradi, A. Kocijan, Hybrid additive manufacturing of Inconel 718 for future space applications, Mater. Charact. 172 (2021), 110842, https://doi.org/10.1016/j.matchar.2020.110842.

[44] R. Sun, Y. Shi, Y. Yang, X. Wang, X. Zhou, Microstructure, element segregation and performance of inconel 625 metal layer deposited by laser assisted ultra-high frequency induction deposition, Surf. Coat. Technol. 405 (2021), 126715, https://doi.org/10.1016/j.surfcoat.2020.126715.

[45] H. Liu, K. Guo, J. Sun, H. Shi, Effect of nb addition on the microstructure and mechanical properties of inconel 718 fabricated by laser directed energy deposition, Mater. Charact. 183 (2022), 111601, https://doi.org/10.1016/j.matchar.2021.111601.

[46] Chapter 8 friction: mechanisms and analysis, in: A. Dorinson, K.C. Ludema (Eds.), Mech. Chem. Lubr, Elsevier, 1985, pp. 149–177, https://doi.org/10.1016/S0167-8922(08)70847-2.

[47] ASTM Standard G102-89(2015)e1, Standard Practice for Calculation of Corrosion Rates and Related Information From Electrochemical Measurements, ASTM International, West Conshohocken, PA, 2015, https://doi.org/10.1520/G0102-89R15E01.